

This is a non-peer reviewed pre-print submitted to EarthArXiv. This manuscript has been submitted to Journal of Advances in Modeling Earth Systems for peer review.

Subsequent versions of this manuscript may have slightly different content.
We welcome feedback. Please contact Riovie Ramos (ramosr34@wpunj.edu)
regarding this manuscript's content.

23 **Abstract**

24 Cloud and convective parameterizations strongly influence uncertainties in equilibrium climate
25 sensitivity (ECS). We provide a proof-of-concept study to constrain these parameterizations in a
26 perturbed parameter ensemble of the atmosphere-only version of the Goddard Institute for Space
27 Studies (GISS) Model E2.1 simulations by evaluating model biases in the present-day runs using
28 multiple satellite climatologies and by comparing simulated $\delta^{18}\text{O}$ of precipitation ($\delta^{18}\text{O}_p$), known
29 to be sensitive to parameterization schemes, with a global database of speleothem $\delta^{18}\text{O}$ records
30 covering the Last Glacial Maximum (LGM), mid-Holocene (MH) and pre-industrial (PI) periods.
31 Relative to modern, paleoclimate simulations show greater sensitivity to parameter changes,
32 allowing for an evaluation of model uncertainties over a broader range of climate forcing and the
33 identification of parts of the world that are parameter sensitive. Certain simulations reproduced
34 absolute $\delta^{18}\text{O}_p$ values across all time periods and LGM and MH $\delta^{18}\text{O}_p$ anomalies relative to the
35 PI better than the default parameterization. Not a single set of parameterizations worked well in
36 all climate states, likely due to the non-stationarity of cloud feedbacks under varying boundary
37 conditions.

38

39 **Plain Language Summary**

40 Equilibrium climate sensitivity (ECS) is a key climate metric that quantifies the rise in global
41 mean surface temperature in response to doubling of atmospheric CO_2 relative to pre-industrial
42 levels. Changes in hydroclimate, temperature extremes, and other aspects of the climate system
43 in future projections, as well as mitigation and adaptation decisions, are closely tied to a model's
44 ECS. For decades, estimates of ECS have remained wide despite improvements from using
45 multiple lines of evidence. One persistent source of this spread is related to cloud and convective

46 processes, which occur at scales too small to be explicitly resolved, and thus require
47 parameterizations to be represented in climate models. These parameterizations directly
48 influence water isotopes by modulating simulated cloud cover, rainfall and atmospheric
49 circulation, and thus can be used to constrain model processes and identify model biases. In this
50 study, we first demonstrate that paleoclimate simulations including the Last Glacial Maximum
51 (LGM), mid-Holocene (MH) and pre-industrial (PI) periods are more parameter sensitive than
52 the modern, covering wider regions of the world that can discriminate among perturbed
53 parameter ensemble members, thus, highlighting the potential of paleo-simulations in better
54 constraining cloud and convective parameterizations. We then identified the top performing
55 parameterization using multiple satellite climatologies and proxy-model comparisons using the
56 oxygen isotope of precipitation where we considered the sensitivity of a proxy site to parameter
57 changes. Our proxy-model comparisons (i.e., absolute values) show an excellent agreement in all
58 runs and time periods but two parameterizations, also supported by the satellite analysis,
59 emerged to perform better than the default GISS parameterization. We also find that simulations
60 are able to capture broad scale LGM-PI and MH-PI oxygen isotope of precipitation patterns,
61 with the latter showing reduced model skill. Similar to the absolute value comparisons, the best
62 parameterization differ for each time period likely due to varying cloud feedbacks under diverse
63 climatic forcing. Overall, our results provides a framework for fine-tuning model representations
64 using paleoclimate data which provides a unique opportunity to assess model uncertainties over a
65 broader range of climate variability than is afforded by the instrumental period and identifying
66 target regions where future archive and proxy development may be most valuable.

67

68 **1 Introduction**

69 Cloud and convective processes vary at scales significantly smaller than a general
70 circulation model (GCM) grid box, requiring them to be parameterized on simulated grid-scale
71 variables (Boucher *et al.*, 2013). Such parameterizations employ different assumptions (Lopez,
72 2007) and thus representation of cloud and convective effects in climate models inherently hold
73 large uncertainties. Cloud and convective parameterizations, aside from aerosol schemes and
74 aerosol-cloud interactions (Meehl *et al.*, 2020), are considered the leading source of inter-model
75 spread in equilibrium climate sensitivity (ECS) estimates (Dufresne and Bony, 2008; Sherwood
76 *et al.*, 2014; Webb *et al.*, 2015; Zelinka *et al.*, 2020) and consequently, the broad range of future
77 climate projections (Flato *et al.*, 2013; Sherwood *et al.*, 2014). The latest generation of climate
78 models participating in Coupled Model Intercomparison Project Phase 6 (CMIP6) have an
79 average ECS value of 3.9°C and range from 1.8°C to 5.6°C (Zelinka *et al.*, 2020), which is
80 higher and more variable than the CMIP5 models (i.e., mean of 3.3°C and range of 1.5°C to
81 4.5°C (Flato *et al.*, 2013; Knutti *et al.*, 2017)) and estimates from Intergovernmental Panel on
82 Climate Change Assessment Report 6 (i.e., mean of 3°C with a very likely range of 2°C to 5 °C,
83 (IPCC, In Press)). Constraining cloud and convective parameterizations may potentially help
84 narrow ECS uncertainties.

85 A perturbed parameter ensembles (PPE) experiment, which creates different versions of
86 a climate model by systematically changing a parameter value within a reasonable range, is
87 particularly useful in assessing how much of the uncertainties are explained by parameter
88 choices. Typically, clouds and convective parameterizations are chosen based on the bias score
89 between the climate model and an observational dataset, usually from satellite remote sensing
90 which dates back to 1994 (Mauritsen *et al.*, 2012; Galewsky *et al.*, 2016). However, in the

91 context of future climate change, these observational datasets only offer a fraction of the range of
92 climate change projected over the next 100 years. Finding ways to constrain these choices on a
93 broader variety of climates is thus desirable. Moreover, in a traditional PPE approach, models
94 are not typically re-tuned into radiative balance after altering a single tuning parameter (Schmidt
95 *et al.*, 2017), which may have important implications in resolving or revealing biases from
96 previous compensating errors (Collins *et al.*, 2011). However, not much is known whether this
97 tuning approach after each parameter change is preferable especially when considering a broader
98 range of climate states.

99 Widely observed through satellites and preserved on various paleoclimate archives, water
100 isotopes provide a common means to understand present and past climates. Water isotopes serve
101 as integrative tracers of the hydrologic cycle due to molecular differences in mass that drive
102 fractionation during water phase changes. In the atmosphere, the variability in the oxygen
103 isotopic composition of precipitation ($\delta^{18}\text{O}_p$) is driven by several local and non-local processes
104 including the origin and initial isotopic composition of the water vapor in an air parcel, amount
105 of rainout, evaporation of rainfall, seasonality and temperature history, and mixing with other air
106 parcels (Dansgaard, 1964; Galewsky *et al.*, 2016; Gat, 1996; Noone, 2008). Increasingly
107 incorporating water isotopes in model simulations has significantly advanced our understanding
108 of the mechanisms that govern their variability in broader spatiotemporal scales (Galewsky *et al.*,
109 2016).

110 Previous studies have demonstrated the sensitivity of water isotope ratios to perturbations
111 in cloud and convective parameterizations in isotope enabled GCMs, signifying their utility in
112 evaluating model performance and potentially identifying model biases (Bolot *et al.*, 2013; Bony
113 *et al.*, 2008; Field *et al.*, 2014; Lee *et al.*, 2009; Schmidt *et al.*, 2005; Nusbaumer *et al.*, 2017).

114 For example, excessive diffusive advection and high convection frequency were shown to cause
115 significant model biases in the isotope enabled Laboratoire de Météorologie Dynamique Zoomed
116 version 4 (LMDZ4, (Risi *et al.*, 2012)) and Community Atmosphere Model version 5 (CAM5,
117 (Nusbaumer *et al.*, 2017)) models, respectively. In the atmosphere-only version of Goddard
118 Institute for Space Studies (GISS) Model E2, water isotopes were found to be more sensitive to
119 parameter changes than traditional diagnostics such as precipitation and temperature, likely
120 related to cumulus entrainment strength (Field *et al.*, 2014). These models were compared
121 against modern water isotope observations from satellites (e.g., Aura Tropospheric Emission
122 Spectrometer (TES), (Worden *et al.*, 2007)); Scanning Imaging Absorption Spectrometer for
123 Atmospheric Cartography (SCIAMACHY), (Frankenberg *et al.*, 2009)), providing a spatially
124 robust means of constraining model results.

125 Variability in water isotopes may also be obtained from various paleoclimate archives
126 that are not only spatially well-distributed but are also available across timescales drastically
127 different from today, such as the Last Glacial Maximum (LGM; 21 ka, or kilo-years before
128 present) and mid-Holocene (MH; 6 ka) periods. The LGM corresponds to a time when global ice
129 volume was at its maximum and greenhouse gas concentrations were lower than today, both
130 driving major changes in the atmosphere compared to present conditions (Pausata *et al.*, 2011;
131 Kageyama *et al.*, 2021; Tierney *et al.*, 2020b). During the MH, insolation is seasonally amplified
132 in the Northern Hemisphere, with larger winter-to-summer temperature differences and
133 associated changes in the hydrological cycle (Brierley *et al.*, 2020; Otto-Bliesner *et al.*, 2006).
134 Performing proxy-model comparison across these contrasting time periods thus allows for
135 evaluating model performance over the full range of hydroclimatic variability in the Earth
136 system.

137 One excellent source of past hydroclimatic information are speleothems. Speleothems are
138 secondary cave deposits that form from dissolution of carbonate bedrock through water action.
139 While their geographical distribution is largely constrained by the geology of a region,
140 speleothems form under a broad range of hydroclimatic regimes ideal for investigating
141 predominant regional patterns. Variations in speleothem $\delta^{18}\text{O}$ largely reflects the $\delta^{18}\text{O}$ of soil
142 ($\delta^{18}\text{O}_s$) and groundwater percolation, which in turn is heavily influenced by $\delta^{18}\text{O}_p$ above the cave
143 and other processes within the karst system (Fairchild and Baker, 2012; Lachniet, 2009). Early
144 speleothem $\delta^{18}\text{O}$ compilations and the more recently available Speleothem Isotope Synthesis and
145 Analysis (SISAL) database (Atsawawaranunt *et al.*, 2018; Comas-Bru *et al.*, 2020, 2019), a large
146 global compilation of speleothem isotope records since the last glacial, have aided in evaluating
147 GCM performance across the LGM and MH time periods (Caley *et al.*, 2014; Cauquoin *et al.*,
148 2019; Comas-Bru *et al.*, 2019; Werner *et al.*, 2016) and have served as an independent validation
149 check in reconstructions of glacial temperature fields (Tierney *et al.*, 2020a), demonstrating their
150 usefulness in benchmarking isotope enabled paleoclimate simulations. However, not all parts of
151 the world are equally influenced by cloud and convective parameter changes, implying that
152 proxy record locations may be more or less constraining against simulations. This has not been
153 fully quantified in existing paleoproxy-model comparisons and/or analyses of model-satellite
154 discrepancies both globally and restricted to proxy sites only.

155 In this study, we explore cloud and convective parameterizations (Table 1) in the GISS-
156 E2.1 climate model (Kelley *et al.*, 2020) that likely have a significant impact on water isotope
157 distribution and ECS. We use two sets of atmosphere-only simulations: one that has been re-
158 tuned into radiative equilibrium in the pre-industrial (hereafter referred to as the balanced
159 version) and another which only changes the parameters (hereafter referred to as the unbalanced

160 version), to evaluate whether this approach is preferable in simulations of past climates with
161 large differences in radiative forcing. We investigate the variability and sensitivity of key climate
162 variables to cloud and convective changes and identify parameter-sensitive sites in the present-
163 day (PD, year 2000) and paleoclimate simulations covering the pre-industrial (PI, 0 ka), MH and
164 LGM periods. We also compare and evaluate the model simulations against multiple satellite
165 climatologies and assess the agreement between simulated $\delta^{18}\text{O}_p$ and speleothem $\delta^{18}\text{O}$ from the
166 SISAL version 2 (SISALv2, Comas-Bru *et al.*, 2020) database. This proof-of-concept study
167 presents a basis to which we determine the best suite of parameters representing clouds and
168 convective processes across distinct time periods, critical in improving isotope-enabled models
169 and thus, ECS and climate projections.

170
171

Table 1. Parameter space exploration of GISS-E2.1.

Short Name	Parameter	GISS-E2.1 default	New Value	Mean Surface Air Temperature, °C (global, NH, SH)	Mean Precipitation, mm/day (global, NH, SH)	Radiation balance at TOA, W/m ² (PI, MH, LGM)
<i>std</i>	standard	----	----	13.99,14.31,13.67	2.96,2.88,3.03	0.098,0.663,-1.92
<i>rev</i>	rain re-evaporation above cloud base	On (1)	Off (0)	13.80,14.04,13.53	0.63,0.63,0.62	0.013,0.094,1.46
<i>entr50-50</i> <i>entr60-40</i> <i>entr20-80</i>	entrainment rate for plume (1 & 2)	0.4; 0.6	0.5; 0.5 0.6; 0.4 0.2; 0.8	13.98,14.29,13.66 14.02,14.33,13.70 14.00,14.28,13.72	2.98,2.90,3.06 2.95,2.87,3.02 2.91,2.82,3.01	0.168,-0.04,-2.00 -0.156,-0.304,-2.20 0.134,0.018,-1.80
<i>tconvadjX2</i>	convection adjustment time	1	2	14.00,14.28,13.72	2.97,2.86,3.06	0.107,-0.062,-2.08
<i>trigger1.1</i> <i>trigger1.2</i> <i>trigger0.99</i> <i>trigger1.3</i> <i>trigger1.0</i>	convective trigger	2	1.1 1.2 0.99 1.3 1.0	13.96,14.29,13.63 13.96,14.29,13.62 13.98,14.30,13.66 13.97,14.28,13.66 13.98,14.30,13.66	2.98,2.90,3.06 2.98,2.90,3.06 2.98,2.89,3.06 2.98,2.91,3.05 2.98,2.90,3.06	0.289,0.061,-1.98 0.289,0.162,-1.98 0.046,-0.101,-2.11 0.289,0.162,-1.98 0.047,-0.101,-2.11
<i>droprad50-50</i> <i>droprad50-130</i> <i>droprad130-50</i> <i>droprad30-130</i>	cloud droplet radius (liquid- ice)	1; 1	0.5; 0.5 0.5; 1.3 1.3; 0.5 1.3; 1.3	13.87,14.11,13.62 14.17,14.52,13.82 13.76,14.00,13.53 14.01,14.36,13.67	2.87,2.76,2.98 2.91,2.81,3.00 2.97,2.89,3.05 2.99,2.91,3.06	-0.194,-0.52,-2.92 0.249,0.067,-1.54 -0.164,-0.475,-2.96 0.032,-0.625,-1.80

<i>critQ2-2</i>	critical cloud water content (liquid & ice)	2; 1	2; 2	14.00,14.32,13.68	2.96,2.86,3.05	0.085,-0.153,-2.12
<i>critQ1-0.5</i>			1; 0.5	14.00,14.34,13.67	2.99,2.90,3.08	0.181,0.135,-1.92
<i>critQ1-4</i>			1; 4	13.95,14.26,13.64	2.96,2.87,3.06	-0.020,-0.168,1.13
<i>critQ2-4</i>			2; 4	13.96,14.30,13.63	2.95,2.85,3.05	0.142,-0.04,-2.23

172

173 2 Materials and Methods

174 2.1 NASA GISS E2.1

175 Simulations were conducted using the atmosphere-only GISS-E2.1, a CMIP6 submission
176 described in length in Kelley et al. (2020). Relative to GISS-E2 (Schmidt *et al.*, 2014), the
177 default E2.1 configuration has an improved treatment of mixed-phase clouds, improvements in
178 the planetary boundary layer parameterization, and systematic increases in convective
179 entrainment rates (Kelley *et al.*, 2020), though these rates are perturbed as part of this study as
180 detailed below.

181 Water tracers ($^1\text{H}_2^{16}\text{O}$, “normal” water; $^2\text{H}^1\text{H}^{16}\text{O}$, δD ; and $^1\text{H}_2^{18}\text{O}$, $\delta^{18}\text{O}$; where permil
182 (‰) $\delta \equiv 1000 * [(R_{\text{std}}/R_{\text{smow}})-1]$) were included in the land surface, sea ice, sea surface, and
183 atmosphere. These isotopes are tracked through all stages of the water cycle and are advected
184 like water through the model with appropriate fractionation during each phase change (LeGrande
185 and Schmidt, 2009; Schmidt *et al.*, 2005, 2007).

186

187 2.2 Time slice experiments

188 We performed three paleo-time slice experiments as described for the LGM (Kageyama
189 *et al.*, 2021, 2017), MH (Otto-Bliesner *et al.*, 2017) and PI (Eyring *et al.*, 2016). These followed
190 the Paleoclimate Modelling and Intercomparison Project (PMIP4) and CMIP6 protocols
191 (Kageyama *et al.*, 2017; Otto-Bliesner *et al.*, 2017). For each time slice, appropriate changes to
192 topography, bathymetry, and land-ocean-ice mask (LGM: Glac1D, Abe-Ouchi *et al.*, 2013;

193 Briggs *et al.*, 2014; Tarasov and Peltier, 2002; Tarasov *et al.*, 2012); river routing (Licciardi *et*
194 *al.*, 1998, 1999; Peltier, 2004); vegetation cover (Ray and Adams, 2001); orbital changes (Berger
195 and Loutre, 1991); greenhouse gases (Indermühle *et al.*, 1999); standard mean ocean water,
196 salinity and water isotopes (Fairbanks, 1989) were made (Table 2). All these runs were
197 completed to surface equilibrium in GISS-E2.1-G (Kelley *et al.*, 2020); the surface sea ice
198 fraction, sea ice thickness, and sea surface temperatures were then recorded. Coupled simulations
199 are computationally expensive, and thus, surface conditions were used in this proof-of-concept
200 study to drive a new suite of GISS-E2.1 simulation (CMIP6) in atmosphere-only mode with the
201 same forcing conditions to create the LGM, MH and PI runs. We conduct one further present-
202 day (PD) experiment to facilitate comparison with the satellite products, using year 2000
203 atmospheric constituents and a climatological mean from Hadley for 2000-2015 for ocean
204 surface conditions (Table 2).

205
206 **Table 2.** Summary of forcing and boundary conditions for each time slice experiment. All experiments
207 applied topography, bathymetry, land-ocean-ice mask, greenhouse gas, river routing and appropriate
208 SMOW changes.

Time slice	Ice sheet	SST/SICE	GHG	Mean salinity, psu	SMOW ($\delta^{18}\text{O}$, δD)
Present Day	modern	Hadley Obs	year 2000	34.7	0‰, 0‰
PI, 0 ka	modern	CMIP6: PI	year 1850	34.7	0‰, 0‰
MH, 6 ka	modern	CMIP6: MH	6 ka	34.7	0‰, 0‰
LGM, 21 ka	Glac1D	CMIP6: LGM	21 ka	35.7	1.0‰, 8.0‰

209

210 2.3 Cloud and convective parameterizations and model tuning

211 GISS-E2.1 regularly uses five tuning parameters (Kelley *et al.*, 2020). Here, we re-tuned
212 the model by altering cloud reflectivity (Schmidt *et al.*, 2017), after each parameter change to
213 ensure that the decadal top of the atmosphere net planetary radiation is within 0.2 W/m² during a
214 pre-industrial simulation (i.e., balanced version). We conduct a parallel set of experiments where
215 this tuning was not done (i.e., unbalanced version) to check that the tuning itself is not

216 influencing our interpretation. Ideally, this positions us to complete fully coupled simulations to
217 explore the full range of variability imparted by these clouds and convective changes during the
218 paleoclimate simulations. However, these experiments are computationally expensive, and
219 beyond the scope of this proof-of-concept study (but are planned in the future). The practical
220 consequence is that variability over the ocean especially is throttled, and the climate system
221 during the paleoclimate runs may no longer be in radiative equilibrium (a symptom of the
222 incomplete climate response to the strong paleoclimate forcing perturbed parameter runs); we
223 note the net top of the atmosphere radiative balance of each simulation (Table 1).

224 The basic structure of the clouds and convection schemes are described in (Del Genio,
225 2012; Del Genio *et al.*, 2015; Kim and Kang, 2012). We have chosen here to explore six
226 different parameters utilized in the cloud and convection schemes that likely have a substantive
227 impact on ECS as well as water isotope distribution (Table 1). A total of 19 simulations were
228 performed for each time period. Parameters chosen are ones not directly constrained by current
229 in situ or satellite observing platforms.

230 Rain re-evaporation above the cloud base (*rev*) has been a parameter previously
231 considered for change because it improves convection and variability (e.g., Madden-Julian
232 Oscillation in Kim and Kang, (2012)). This parameter makes the GISS-2.2 model distinct from
233 the GISS-2.1 (Rind *et al.*, 2020). Water isotopes are sensitive to changing this parameter (Field
234 *et al.*, 2014). Increasing this parameter results in additional atmospheric moistening and a
235 subsequent increase in precipitation over the Maritime Continent (i.e., increased bias); however,
236 it does improve isotopic matches between GISS-E2.1 simulations and satellite observations
237 (Worden *et al.*, 2007).

238 The entrainment rate (*entr*) parameters control how much environmental mass is
239 entrained into a less- and more-entraining convective plume. At most, two updraft plumes are
240 permitted to initiate at each model level in the GISS convective scheme, and the only
241 requirement is that they have different entrainment rates thus allowing a representation of
242 shallow (i.e., more entraining) and deep (i.e., less entraining) convective towers within any
243 convective cloud ensemble in the GCM grid box.

244 The convective adjustment time (*tconvadj*) is a parameter that controls how quickly
245 convective mass reaches the tropopause, and thus how quickly the environmental profile of
246 temperature and moisture adjusts to moist convective processes.

247 The convective trigger (*ctrigger*) parameter determines what environmental conditions
248 are necessary for initiating convection. Physically this parameter can be interpreted as
249 accounting for the multi-faceted role that the planetary boundary layer plays in convective
250 initiation (e.g., turbulent lifting of parcels, variations in near-surface stability or moisture across
251 a grid box), the role of vertical wind shear, the role of mesoscale ascent causing local
252 destabilization, or the role of gravity waves in the weakening of convection-inhibiting stable
253 layers.

254 The radius multiplier (*droprad*) is a parameter that governs the sizes of liquid droplets
255 and ice particles for a given condensate amount. Though there are some observational estimates
256 of sizes at cloud tops, within-cloud estimates are largely unconstrained (and particularly within
257 convection, where attenuation of radiometric signals are substantial). In general, smaller sizes
258 result in clouds reflecting more shortwave radiation coincident with reduced outgoing longwave
259 radiation.

260 Auto-conversion of cloud water content to precipitation is governed by a critical cloud
261 water content scaling parameter ($critQ$). Any liquid or ice water content above the scaled critical
262 threshold will be converted to precipitation via auto-conversion, thus affecting cloud condensate,
263 cloud fractions, and in turn, radiation.

264

265 2.4 Satellite data

266 Our perturbed parameter configurations are balanced and evaluated using multiple
267 present-day satellite climatologies provided by the Obs4MIPS project ([https://esgf-
269 node.llnl.gov/projects/obs4mips/](https://esgf-
268 node.llnl.gov/projects/obs4mips/)) hosted on the Earth System Grid Federation
(<https://esgf.llnl.gov>). Top of the atmosphere absorbed shortwave (SWabsTOA) and outgoing
270 longwave radiation (OLR), along with cloud radiative forcing estimates (SW_CRE, and
271 LW_CRE) are provided by the CERES EBAF Edition 4.1 product (Kato *et al.*, 2018; Loeb *et al.*,
272 2018, 2020). Temperature and water vapor profiles are provided by AIRS Version 6 retrievals
273 (Tian *et al.*, 2019; Tian and Hearty, 2020) for altitudes at and below 600 hPa, and by MLS
274 Version 4 satellite retrievals (Waters *et al.*, 2006) at and above 200 hPa. Column integrated total
275 (cloud plus precipitating) liquid water estimates (TLWP) are provided by the MAC-LWP
276 (Elsaesser *et al.*, 2017) and TRMM 3A12 (Kummerow *et al.*, 2001) products, while the column
277 integrated ice counterparts (TIWP) are provided by the CloudSat 2C-Ice (Deng *et al.*, 2015) R05
278 and MODIS C6 (Marchant *et al.*, 2016; Platnick *et al.*, 2015; Yi *et al.*, 2017) products. Total
279 precipitation (prec) is provided by GPCP Version 2.3 (Adler *et al.*, 2003) and TRMM TMPA
280 (Adler *et al.*, 2009; Huffman *et al.*, 2007) Version 7 products. Convective precipitation
281 (prec_mc) is provided by the GPM Dual-frequency Precipitation (DPR) Radar product (Iguchi *et*
282 *al.*, 2012). Global total cloud cover (tcc_isccp) is provided by the ISCCP (Rossow and Schiffer,

283 1999) D1 total cloud fraction product, while surface wind estimates are provided by the
284 QuikSCAT satellite and Remote Sensing Systems surface wind products (Wentz and Schabel,
285 2000; Wentz *et al.*, 2007).

286 We compared these multiple satellite climatologies to the perturbed parameter
287 simulations and computed both global and proxy site-averaged root mean square error (RMSE)
288 scores.

289

290 2.5 Paleoclimate data

291 To evaluate the atmosphere-only $\delta^{18}\text{O}_p$ simulations, we used land-based paleoclimate
292 constraints which are less impacted by the lack of surface ocean and ice feedbacks in these runs,
293 minimizing proxy-model mismatches that may be expected from including ice core records. We
294 use the latest Speleothem Isotope Synthesis and Analysis (SISAL) version 2 database (Comas-
295 Bru *et al.*, 2020) and extracted 378 speleothem records from a total of 224 unique sites. In this
296 version, multiple age models for most cave sites were generated but we used the original
297 published chronologies in obtaining mean $\delta^{18}\text{O}$ over the following time periods: LGM (21 ± 1
298 ka), MH (6 ± 1 ka) and PI (last 2 ka). Depending on the mineralogy (i.e., calcite or aragonite),
299 mean $\delta^{18}\text{O}$ values (VPDB) were converted to their drip water equivalents analogous to $\delta^{18}\text{O}_p$
300 (VSMOW) (Comas-Bru *et al.*, 2019). We used model-generated mean annual SAT extracted at
301 the grid points nearest the cave sites as representative for cave temperatures required in the drip
302 water conversion. Records where mineralogy is unknown or mixed were excluded. Multiple
303 records in a single site and model grid box were then averaged except for those that report large
304 dating errors (e. g., Kesang Cave, (Cai *et al.*, 2017)). A total of 257, 195 and 81 records were
305 obtained for the PI, MH and LGM periods, respectively.

306

307 2.6 Sensitivity to perturbations and proxy-model comparison

308 To assess the spatial sensitivity of $\delta^{18}\text{O}_p$ to perturbations in cloud and convective
309 parameterizations, we derived z-scores for each experiment, $z = \frac{(x-\mu)}{\sigma}$; where x is the mean
310 $\delta^{18}\text{O}_p$ of an ensemble member, μ is the PPE mean and σ is the standard deviation greater than the
311 mean decadal variability of each experiment per grid box. We counted the number of ensembles
312 per grid box where the absolute value of the z-score is greater than 1 and then normalized the
313 total against the number of PPE runs to derive a sensitivity score. A maximum score of 1
314 indicates that all 19 ensemble members show significant difference from the PPE mean, and thus
315 the highest sensitivity to parameter changes. We similarly evaluated the spatial sensitivity of
316 PREC and SAT to parameter changes.

317 Simulated $\delta^{18}\text{O}_p$ were extracted from the nearest grid points to the cave sites and
318 compared with that of the proxy for each period, and time slice anomalies with PI as the
319 baseline. Skill statistics were calculated over each time period using a weighted least square
320 regression. The weights applied to the extracted grid points were from the derived sensitivity
321 scores of a $\delta^{18}\text{O}_p$ grid box to changes in cloud and convective parameterizations to highlight the
322 strength of a proxy site in discriminating among perturbations.

323

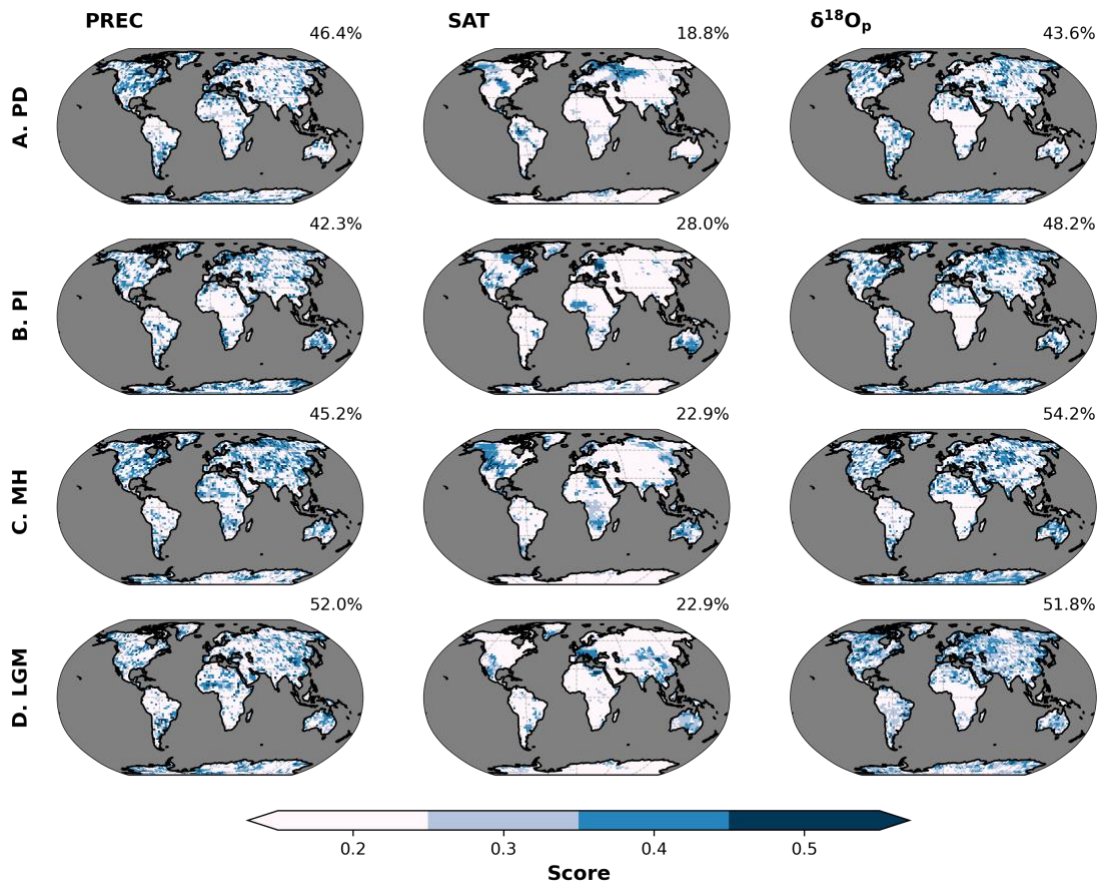
324 **3 Results**

325 3.1 Spatial sensitivity to perturbations in clouds and convective parameterizations

326 Based on the resultant spatial variability of precipitation (PREC), surface air temperature
327 (SAT), and $\delta^{18}\text{O}_p$ (Text S1 in the supporting information), we derived scores that represent the
328 number of ensembles per grid box showing significant difference from the PPE mean (see

329 Section 2.6) to highlight spatial sensitivity to parameterization choices. Using the simulations
 330 from the balanced version, PREC and $\delta^{18}\text{O}_p$ are more sensitive to parameter changes, with nearly
 331 50% of the overall land surface showing significant difference from the mean across all time
 332 periods (Figure 1). SAT, on the other hand, show less sensitivity, covering less than 30% of the
 333 total land surface.

334
 335



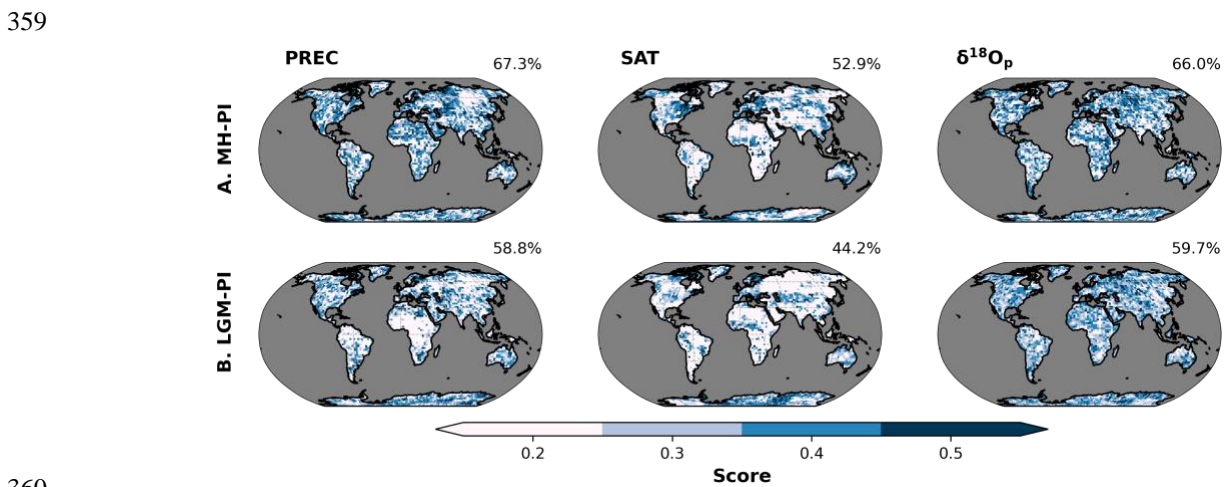
336
 337
 338
 339
 340
 341
 342
 343
 344

Figure 1. Spatial sensitivity of precipitation (PREC), surface air temperature (SAT), and $\delta^{18}\text{O}_p$ to perturbed cloud and convective parameters for different time periods (a-d). Shading represents the scores or the fraction of the total number of ensembles per grid box showing significant difference from the PPE mean. The higher the score, the more sensitive a location is to parameter changes. The oceans are masked to highlight changes on land for these atmosphere-only simulations. Percentages reported at the top right of each panel indicate the fraction of land surface (using PD configuration) having a score greater than 0.2.

345 The regions that are *most* sensitive to clouds and convective processes in the GISS-E2.1
 346 simulations of SAT are spatially varying across time periods while that of PREC and $\delta^{18}\text{O}_p$ are
 347 located away from deep convection zones (Figure 1). Sensitive regions consistently include
 348 North America, subtropical South America, Europe, western and northern Africa, north Asia,
 349 middle East, and Australia across time periods, forming the key sites to which model results may
 350 be principally constrained by the presence of viable paleo-proxy records.

351 Relative to the PI period, sensitive regions for each variable increase in extent in the MH
 352 and LGM periods (Figure 2), indicating that paleoclimate simulations are more sensitive to
 353 parameter changes relative to the modern, supporting the premise of this proof-of-concept study
 354 that paleoclimate simulations may be better at discriminating cloud and convective
 355 parameterization changes across multiple PPE members than modern.

356 This observation is consistent with that of the unbalanced version, however, the spatial
 357 extent of highly parameter-sensitive sites has decreased across all time periods (Text S1, Figures
 358 S3 and S4 in the supporting information), indicating that tuning can impact model sensitivity.



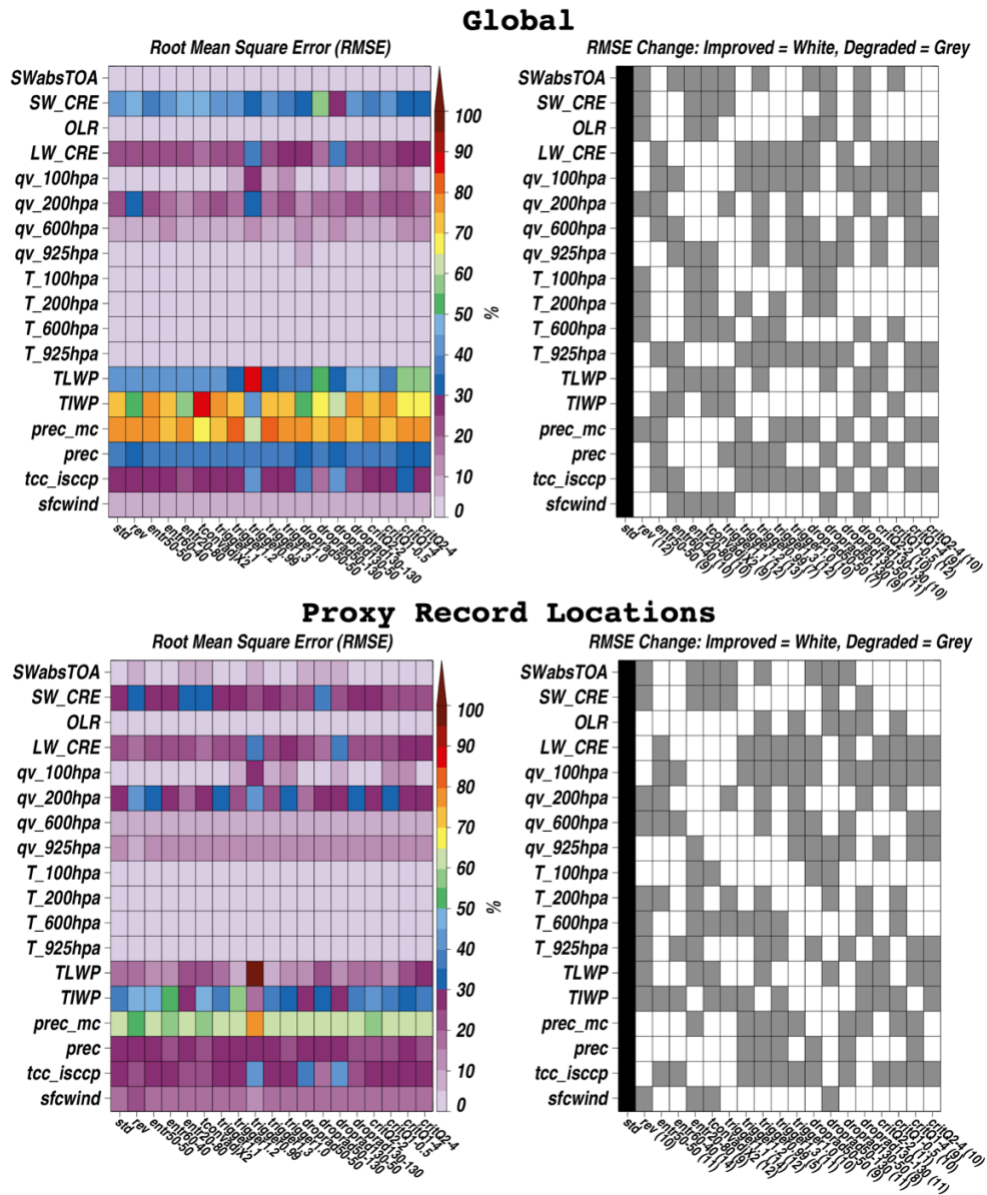
360 **Figure 2.** Spatial sensitivity of precipitation (PREC), surface air temperature (SAT), and $\delta^{18}\text{O}_p$
 361 to perturbed cloud and convective parameters for (a) MH-PI and (b) LGM-PI. Shading represents
 362 the scores or the fraction of the total number of ensembles per grid box showing significant
 363 difference from the PPE mean. The higher the score, the more sensitive a location is to parameter
 364 changes. The oceans are masked to highlight changes on land for these atmosphere-only
 365

366 simulations. Percentages reported at the top right of each panel indicate the fraction of land
367 surface (using PD configuration) having a score greater than 0.2.
368

369 3.2 Model evaluation using multiple satellite climatologies

370 Radiation, cloud, and thermodynamic variables from modern PPE simulations are
371 compared to satellite estimates provided largely from the Obs4MIPS archive (Waliser *et al.*,
372 2020) (see Section 2). It is often the case that inter-product differences for any cloud or
373 thermodynamic variable exceeds published random noise or uncertainty estimates. Such
374 differences arise due to systematic regime-dependent unknowns in satellite cloud and
375 precipitation remote sensing (Duncan and Eriksson, 2018; Elsaesser and Kummerow, 2015; Liu
376 *et al.*, 2017). To avoid root mean square error (RMSE) scores being dependent on any one
377 satellite product choice, we explicitly account for satellite product systematic biases by allowing
378 no contribution to RMSE if the model field falls within the observational range bounded by the
379 minimum and maximum product estimates.

380 RMSE derived for global, as well as for grid boxes co-located only with proxy sites, are
381 shown in Figure 3. Across the board, RMSE is lower with a more muted response across PPE
382 members for proxy site locations, where on average, both total and convective rainfall are a
383 factor of ~ 2 less than most convectively active tropical regions. Less convection implies a
384 smaller reliance on convective and cloud parameterizations, and a less complex atmosphere to
385 simulate. Both *entr60-40* and *tconvadjX2* are most skillful for proxy site PREC, with a 5-10%
386 reduction in RMSE compared to *std*, the default mode for GISS-E2.1; *entr60-40* was the
387 configuration exhibiting subtle improvement across more diagnostics than other PPE members.
388 The top performer changes when considering global scores to *droprad50-50* and *droprad130-50*,
389 with both exhibiting the lowest global RMSE for PREC.



391 **Figure 3.** Comparison of model with satellite data. (top left) Global model-satellite RMSE
 392 scores for absorbed shortwave (SW) radiation at the top of the atmosphere (SWabsTOA), SW
 393 cloud radiative effects (SW_CRE), outgoing longwave radiation (OLR), longwave (LW)_CRE,
 394 water vapor (qv) and temperature (T) at various levels, total (cloud+precipitating) liquid and ice
 395 water paths (TLWP, TIWP), convective and total precipitation (prec_mc, prec), ISCCP satellite
 396 cloud cover (tcc_isccp), and 10-meter surface wind speeds (sfcwind). (top right) binary white-
 397 gray shading indicating if RMSE scores improved for a given ensemble member relative to *std*,
 398 with numbers indicating the number of metrics exhibiting improvement. (bottom row) As in the
 399 top row, but only for model and satellite grid boxes co-located with paleo-proxy sites.
 400
 401

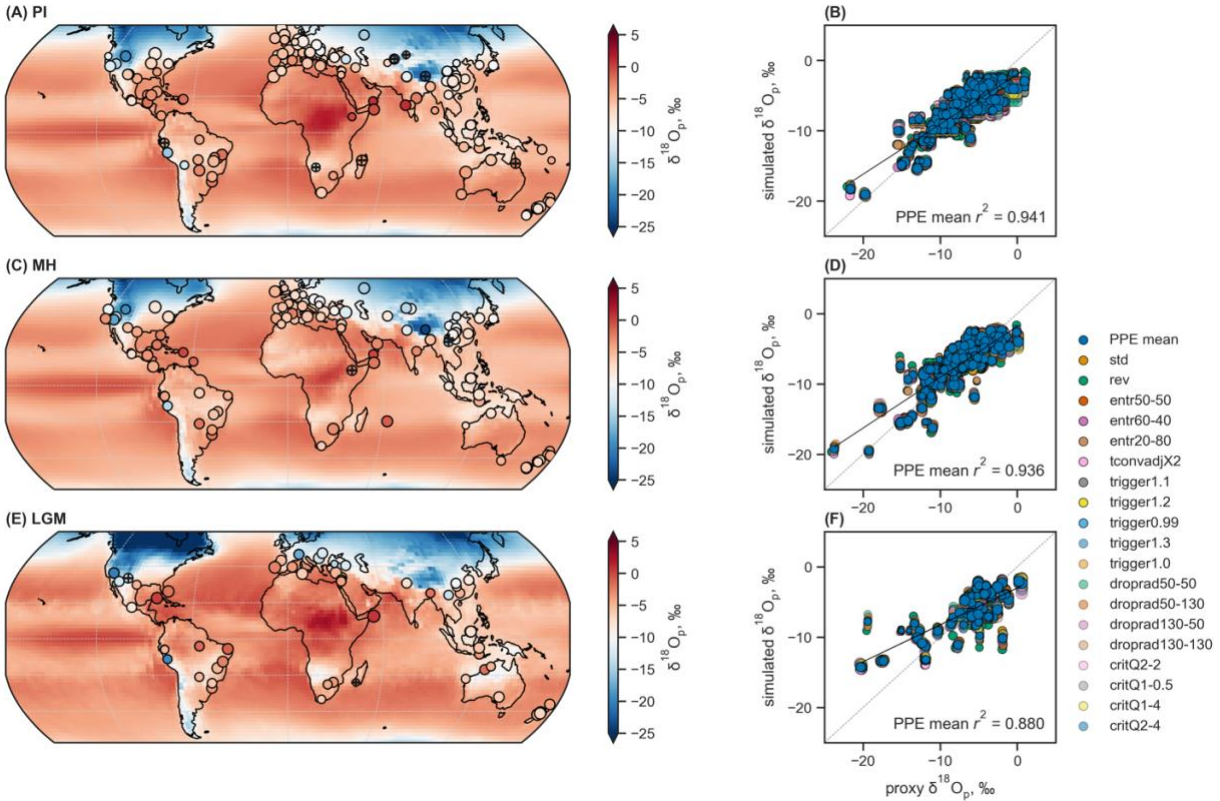
401

402 3.3 Model evaluation using proxy data under PI, MH and LGM conditions

403 Our selected proxy database comprises a total of 257, 195 and 81 records for the PI, MH
404 and LGM periods, respectively. From each of the models, we extracted the simulated $\delta^{18}\text{O}_p$
405 nearest each cave site. As shown in our proxy-model comparisons (Figure 4), the mean $\delta^{18}\text{O}_p$
406 distribution in all runs and time periods are in excellent agreement with the proxies. In these
407 comparisons, we prescribed weights to the simulated $\delta^{18}\text{O}_p$, based on Figure 1, which gives
408 importance to the spatial sensitivity of a particular site to parameter changes. This significantly
409 improved the overall proxy-model agreement compared to the unweighted calculation (Figure
410 S6-a to -s and S7 in the supporting information).

411 While these first order comparisons show excellent agreement, discrepancies remain; for
412 example, simulated $\delta^{18}\text{O}_p$ is more negative (positive) at low (mid- to high) latitude speleothem
413 sites compared to the proxies, with those from the LGM exhibiting the largest offsets (Figure 4).
414 These discrepancies could be due to cave specific factors and model limitations (see Discussion)
415 that may exacerbate proxy-model mismatches. Because simulated $\delta^{18}\text{O}_s$ has the potential to
416 better reflect processes within the karst system, we then compared the proxies with the $\delta^{18}\text{O}_s$
417 model results. Comparisons show high and significant correlations across all time periods
418 (Figure S8 in the supporting information) with the enriched $\delta^{18}\text{O}_s$ values showing a better match.
419 However, the mismatch between the depleted $\delta^{18}\text{O}_s$ values remain leading to an overall lower
420 agreement compared from using simulated $\delta^{18}\text{O}_p$ (Figure S9 in the supporting information).

421



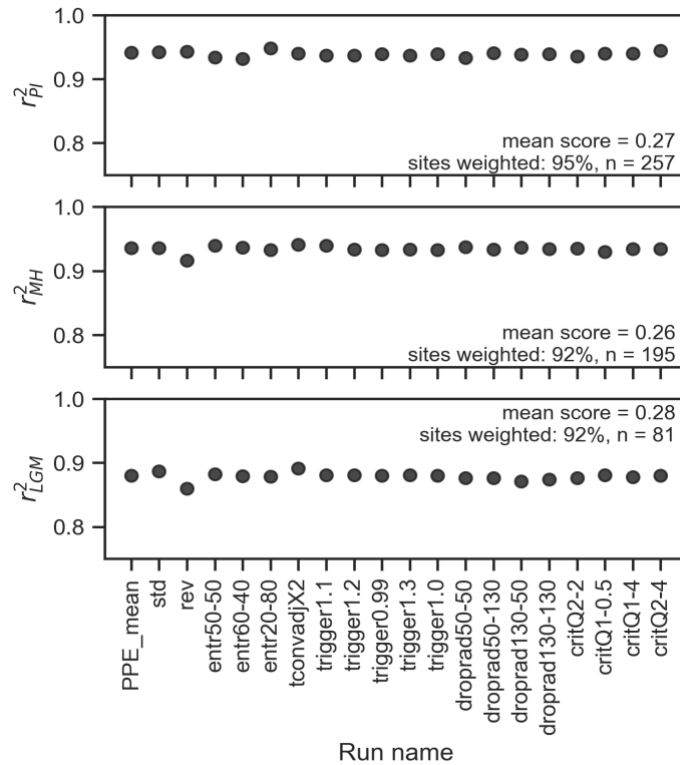
422
 423 **Figure 4.** Comparison of simulated $\delta^{18}\text{O}_p$ with speleothem $\delta^{18}\text{O}$. Global distribution of simulated
 424 $\delta^{18}\text{O}_p$ (background) and speleothem $\delta^{18}\text{O}$, converted to their drip water equivalents (See
 425 Materials and Methods) under (a) PI ($n = 257$), (c) MH ($n = 195$) and (e) LGM ($n = 81$)
 426 conditions. Background and extracted data points are from the PPE mean. SISAL $\delta^{18}\text{O}$ points
 427 with standard deviation greater than 1 are marked with '+'. Scatterplots between simulated and
 428 proxy $\delta^{18}\text{O}_p$ for the respective time periods (b, d, f). PPE members are differentiated by color.
 429 Black lines represent the weighted least squares regression fits to data points while the gray
 430 dashed lines represent the 1:1 line. Weighted r^2 for the PPE mean is reported in the lower right
 431 corner of each scatterplot. The size of the circles in all plots are scaled to the sensitivity scores
 432 derived in Figure 1. Results for each ensemble member are in Figure S6-a to S6-s in the
 433 supporting information.

434

435 Spread among the weighted r^2 values in each parameterization is small (standard
 436 deviation, $\sigma < 0.05$, Figure 5), indicating that the parameterization choices do not drastically
 437 impact $\delta^{18}\text{O}_p$ simulations, consistent with the proxy site-collocated satellite results. Nonetheless,
 438 certain simulations represent an improvement from the *std* run. The entrainment rate for plume
 439 (*entr20-80*) parameterization exhibits the highest skill for the PI period, whereas the convection
 440 adjustment time (*tconvadjX2*) parameterization best represents cloud and convective processes

441 for the MH and LGM periods. Considering only the sites common across the time periods (i.e.,
 442 limited by the number of LGM sites), the *entr20-80* parameterization became one of the poorest
 443 performing models for the PI period. However, another entrainment rate scheme, *entr60-40*,
 444 emerged as the best performing parameterization for PI. The *tconvadjX2* parameterization
 445 remained the best performing scheme for the MH, indicating that the reduced number of data
 446 points did not affect the model evaluation for this time period. These results, broadly consistent
 447 with best performers derived from satellite comparisons (considering only the proxy sites),
 448 suggest that while different cloud and convective scheme settings do not necessarily impose
 449 large changes on the model results for the sites considered, the *best* parameterization for each
 450 time period varies depending upon the boundary conditions.

451

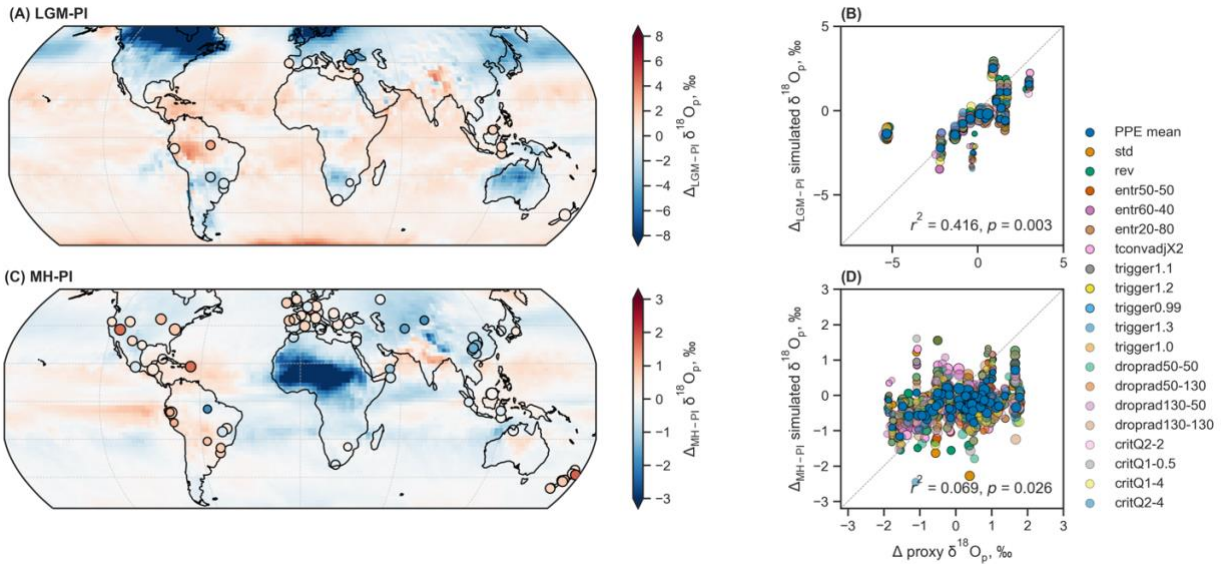


452
 453
 454
 455

Figure 5. Weighted r^2 values between simulated $\delta^{18}O_p$ and SISAL $\delta^{18}O$. All speleothem $\delta^{18}O$ were converted to their drip water equivalent.

3.4 LGM and MH isotopic changes and model performance

To investigate the impact of parameter changes on the relative shift in $\delta^{18}\text{O}_p$, we computed anomalies between the LGM and MH relative to the PI. LGM-PI anomalies consist of 17 records whereas MH-PI anomalies contain 79 records. Similar to the absolute value comparisons, we prescribed weights (extracted from Figure 2) to the simulated $\delta^{18}\text{O}_p$ anomalies. The spatial distribution of simulated LGM-PI $\delta^{18}\text{O}_p$ in the PPE mean shows an overall depletion over land, with the northern latitudes (i.e., ice sheet over North America and Europe) exhibiting the greatest negative $\delta^{18}\text{O}_p$ excursions (Figure 6A). In contrast, the mid-latitudes are only slightly depleted while the Amazon, northern Africa, Himalayas, and oceanic regions show overall positive $\delta^{18}\text{O}_p$ anomalies. Comparison with SISAL $\delta^{18}\text{O}$ anomalies show moderate and statistically significant ($p < 0.011$) proxy-model relationship (Figure 6B, Figure 7) with at least 70% of the records sharing similar signs. The strong positive and negative anomalies observed in Paraiso cave, Brazil, and Sofular cave, Turkey, respectively, are not captured by the models, where simulated $\delta^{18}\text{O}_p$ changes instead show values closer to zero. The spread among the weighted r^2 values remains small ($\sigma < 0.08$, Figure 7). The *tconvadjX2* parameterization outperformed the *std* run, exhibiting the lowest proxy-model mismatch compared to other parameterization results (Figure 7). Notably, this simulation also performed best in the absolute value comparisons for the LGM period.

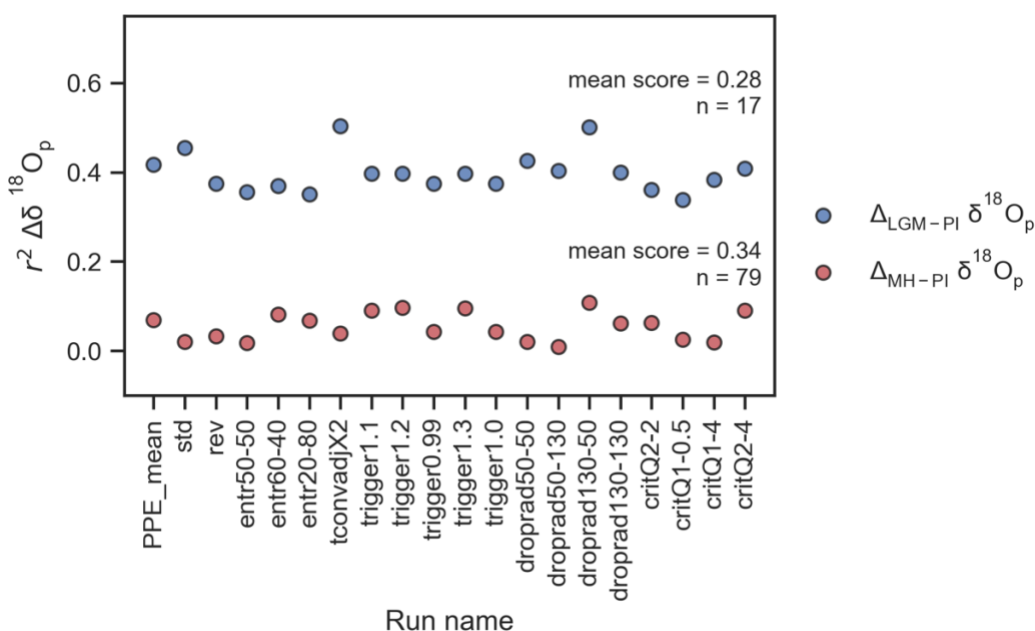


475
 476 **Figure 6.** Comparison of simulated $\delta^{18}\text{O}_p$ anomalies (background) with speleothem $\delta^{18}\text{O}$ (filled
 477 circles) for each time slices: (a) LGM-PI ($n = 17$), (c) MH-PI ($n = 79$). Background and extracted
 478 data points are from the PPE mean. Scatterplots between simulated and proxy $\delta^{18}\text{O}_p$ for the
 479 respective time periods (b, d). PPE members are differentiated by color. Gray dashed lines
 480 represent the 1:1 line. Weighted r^2 for the PPE mean is reported in the lower right corner of each
 481 scatterplot. The size of the circles in all plots are scaled to the sensitivity scores derived in Figure
 482 2. Results for each ensemble member are in Figure S10-a to S10-s in the supporting information.
 483
 484

485 Compared to LGM variations, MH changes relative to PI are more modest. Interior South
 486 America, India and Australia show positive $\delta^{18}\text{O}_p$ anomalies in the PPE mean (Figure 6C). In
 487 contrast, North America, Eurasia, Himalayas, and East Asia show negative $\delta^{18}\text{O}_p$ anomalies,
 488 with the western and central African region showing the greatest negative $\delta^{18}\text{O}_p$ excursions.
 489 Proxy-model agreement across runs lack skill in replicating MH-PI isotopic changes observed in
 490 the SISAL records (Figure 6D, 7), with only 40% of the records showing similar signs in the
 491 PPE mean. Isotopic changes over East Asia and the Maritime Continent are quite robust with
 492 respect to the proxies. The largest deviations are found in North and Central America (South
 493 America) where positive (negative) anomalies are not reflected in the simulated $\delta^{18}\text{O}_p$ changes.
 494 Overall, the magnitude of change is consistently smaller in the simulations (Figure 6D). Of the
 495 19 simulations, only 9 PPE members show statistically significant ($p < 0.04$) relationship,

496 outperforming the *std* $\delta^{18}\text{O}_p$ run (Figure 7). The best performing parameterization is *droprad130-*
 497 *50* (weighted $r^2 = 0.11$, Figure 7), where 59% of the data points now share similar signs. Notable
 498 regions of observed improvement are in Europe and Central Asia (Figure S10 in the supporting
 499 information). Reducing the number of datapoints to match the sites from the LGM-PI changes
 500 shows a different result such that the *critQ2-4* parameterization now shows the highest skill
 501 (weighted $r^2 = 0.45$).

502



503 **Figure 7.** Weighted r^2 values between simulated $\delta^{18}\text{O}_p$ and SISAL $\delta^{18}\text{O}$ anomalies.
 504

505

506 4 Discussion and Conclusions

507 In this study, we have identified parts of the world that are most sensitive to convective
 508 and cloud parameterizations, which may provide the best opportunity for constraining key
 509 metrics in climate models. Parameter-sensitive sites are different between the balanced and
 510 unbalanced versions of the models with the latter showing more regions of lower sensitivity
 511 scores. This is likely related to the greater variability among PPE members induced by random
 512 changes in certain variable fields by the parameter perturbations, affecting more indiscriminate

513 regions in the world. This outcome from the unbalanced version is less useful in constraining
514 biases related to cloud and convective parameterizations.

515 Our satellite-model analyses, stratified by global and proxy-specific skill scores, reveal
516 that the distribution of proxy sites here lie outside of the spatial domains most impacted by cloud
517 and convective parameterization choices. This suggests a need for additional optimally suited
518 sites distributed across more complex convection-cloud schemes to constrain global simulations.
519 Additionally, conducting these experiments using different coupled atmosphere-ocean-vegetation
520 models could provide an excellent framework for targeted paleoclimate fieldwork to develop
521 archives from these convective- and parameter-sensitive areas across the world.

522 Though the proxy sites sample less complex atmospheric scenes, the first order spatial
523 pattern of $\delta^{18}\text{O}_p$ is in excellent agreement between proxy data and all PPE members across all
524 time periods. Also supported by the satellite analyses, two parameterizations with highest model
525 skill emerged: a 20:80 split of entrainment rate for plume (*entr20-80*) for the PI period and
526 doubled convection adjustment time (*tconvadjX2*) for the MH and LGM periods. The
527 simulations are able to capture broad scale LGM-PI $\delta^{18}\text{O}_p$ patterns where *tconvadjX2*
528 parameterization performed best among parameterizations. On the other hand, model skill is
529 significantly reduced in the MH-PI runs where the magnitude of change is consistently smaller in
530 all simulations compared to the proxies.

531 It is highly likely that the coupled simulations of these same experiments will exhibit a
532 greater range of variability across simulations. The fixed SSTs in our runs allowed us the ability
533 to explore this approach with computationally inexpensive simulations; however, it also throttles
534 coupled feedbacks muting LGM and MH variability across ensemble members and precluded us
535 from calculating ECS for every perturbed parameter. Further, these fixed surface ocean

536 conditions limit the paleoclimate constraints to land-based proxy archives. Other potential
537 sources of model discrepancies are related to ice sheet topography changes and dust
538 concentrations (LGM), along with the lack of vegetation and dust concentration feedbacks (LGM
539 and MH) (Crucifix and Hewitt, 2005; Harrison *et al.*, 2014; Masson-Delmotte *et al.*, 2006;
540 Ullman *et al.*, 2014), which may be best evaluated using fully coupled atmosphere-ocean
541 models.

542 Speleothem proxy climate records have their own set of uncertainties. Speleothem $\delta^{18}\text{O}$
543 primarily reflects local and regional climate signals controlling $\delta^{18}\text{O}_p$. However, this signal may
544 be altered as it enters the soil zone and epikarst, a zone that stores infiltrated rainwater, through
545 mixing with existing waters, seasonality of recharge rates, and fractionation by evaporation
546 before reaching the cave system (Baker *et al.*, 2019; Hartmann and Baker, 2017). Within the
547 cave itself, the calcite $\delta^{18}\text{O}$ signal can be further altered by non-equilibrium fractionation
548 processes and temperature-dependent fractionation during speleothem deposition (Baker *et al.*,
549 2019; Hartmann and Baker, 2017; Lachniet, 2009). Using $\delta^{18}\text{O}_s$ instead of $\delta^{18}\text{O}_p$ in the
550 comparisons did not show an improvement either (Figure S8, S9 in the supporting information).
551 These cave specific factors are not reproduced in the models, exacerbating discrepancies
552 between proxies and simulations. Converting speleothem $\delta^{18}\text{O}$ to its drip water equivalent
553 similarly introduces uncertainties as past cave temperatures are unknown (Comas-Bru *et al.*,
554 2019). A natural next step to better comparing the models to proxies is to convert the model
555 output into proxy space via proxy system models, an area of ongoing research (Dee *et al.*, 2017;
556 Evans *et al.*, 2013).

557 While model biases and proxy uncertainties remain, our initial results add to the growing
558 body of work that demonstrates the utility of paleoclimate data in better constraining model skill,

559 particularly at the model development stage (Tierney *et al.*, 2020a, 2020b; Zhu *et al.*, 2019). Our
560 approach and results may be extended to other GCMs and could be especially useful for other
561 models using similar parameters in their cloud and convective parameterization setups. Because
562 cloud feedbacks within the climate system are non-stationary under varying boundary conditions
563 (Zhu *et al.*, 2019), hence leading to differences in which parameterization experiment performs
564 best for each time period, fine-tuning future simulations requires determining all plausible
565 parameter combinations and testing the limits of parameter values used in this study. Future
566 work applying this framework to coupled ocean-atmosphere simulations and incorporating
567 vegetation and dust change is needed to fully investigate the impact of parameter choices on
568 paleoclimate simulations. Incorporation of other land-based water isotope proxies such as those
569 from ice cores, and inclusion of SST proxies which reflects expected changes in radiative
570 balance, will allow for further model evaluation. Techniques like paleoclimate data assimilation
571 could also be leveraged to identify optimal parameter choices that best matches the paleorecord,
572 and subsequently better constrain ECS.

573

574 **Acknowledgments**

575 We thank NASA GISS and the NASA Center for Climate Simulation for institutional
576 support. The satellite data aggregation and analysis contributions by GSE are supported by the
577 NASA Data for Operations and Assessments (NDOA) program (Grant #NNX17AF46G), the
578 Science of Terra, Aqua and Suomi NPP Program (Grant #80NSSC18K1030), and the
579 Precipitation Measurement Missions (PMM) program (RTOP WBS #573945.04.18.03.60). This
580 study was supported by a National Science Foundation Paleo Perspectives on Climate Change
581 (P2C2) Award (Award Number 1805544) to Michael Griffiths.

582
583
584
585
586
587
588
589
590
591
592
593
594
595
596
597
598
599
600
601
602
603

Open Research

Our perturbed parameter configurations were evaluated using multiple present-day satellite climatologies provided by the Obs4MIPS project (<https://esgf-node.llnl.gov/projects/obs4mips/>) hosted on the Earth System Grid Federation (<https://esgf.llnl.gov/>). Top of the atmosphere absorbed shortwave (SWabsTOA) and outgoing longwave radiation (OLR), along with cloud radiative forcing estimates (SW_CRE, and LW_CRE) are provided by the CERES EBAF Edition 4.1 product (Kato *et al.*, 2018; Loeb *et al.*, 2018, 2020). Temperature and water vapor profiles are provided by AIRS Version 6 retrievals (Tian *et al.*, 2019; Tian and Hearty, 2020) for altitudes at and below 600 hPa, and by MLS Version 4 satellite retrievals (Waters *et al.*, 2006) at and above 200 hPa. Column integrated total (cloud plus precipitating) liquid water estimates (TLWP) are provided by the MAC-LWP (Elsaesser *et al.*, 2017) and TRMM 3A12 (Kummerow *et al.*, 2001) products, while the column integrated ice counterparts (TIWP) are provided by the CloudSat 2C-Ice (Deng *et al.*, 2015) R05 and MODIS C6 (Marchant *et al.*, 2016; Platnick *et al.*, 2015; Yi *et al.*, 2017) products. Total precipitation (prec) is provided by GPCP Version 2.3 (Adler *et al.*, 2003) and TRMM TMPA (Adler *et al.*, 2009; Huffman *et al.*, 2007) Version 7 products. Convective precipitation (prec_mc) is provided by the GPM Dual-frequency Precipitation (DPR) Radar product (Iguchi *et al.*, 2012). Global total cloud cover (tcc_isccp) is provided by the ISCCP (Rossow and Schiffer, 1999) D1 total cloud fraction product, while surface wind estimates are provided by the QuikSCAT satellite and Remote Sensing Systems surface wind products (Wentz and Schabel, 2000; Wentz *et al.*, 2007). The water isotope proxies were derived from the Speleothem Isotope

604 Synthesis and Analysis (SISAL) version 2 database (Comas-Bru *et al.*, 2020) and can be
605 accessed through <https://researchdata.reading.ac.uk/256/>.

606

607 **References**

608 Abe-Ouchi, A. *et al.* (2013), Insolation-driven 100,000-year glacial cycles and hysteresis of ice-
609 sheet volume, *Nature*, 500190-193, doi:10.7916/D8MC994B/download.

610 Adler, R. F. *et al.* (2003), The Version-2 Global Precipitation Climatology Project (GPCP)
611 Monthly Precipitation Analysis (1979-Present), *Journal of Hydrometeorology*, 41147-
612 1167.

613 Adler, R. F., Wang, J. J., Gu, G., and Huffman, G. J. (2009), A ten-year tropical rainfall
614 climatology based on a composite of TRMM products, *Journal of the*
615 *Meteorological Society of Japan*, 87A281-293.

616 Atsawawaranunt, K. *et al.* (2018), The SISAL database: a global resource to document oxygen
617 and carbon isotope records from speleothems, *Earth System Science Data*, 101687-1713.

618 Baker, A. *et al.* (2019), Global analysis reveals climatic controls on the oxygen isotope
619 composition of cave drip water, *Nature Communications*, 10(2984), 1-7.

620 Berger, A., and Loutre, M. F. (1991), Insolation values for the climate of the last 10 million
621 years, *Quaternary Science Reviews*, 10(4), 297-317, doi:10.1016/0277-3791(91)90033-Q.

622 Bolot, M., Legras, B., and Moyer, E. J. (2013), Modeling and interpreting the isotopic
623 composition of water vapor in convective updrafts, *Atmospheric Chemistry and Physics*,
624 137903-7935.

625 Bony, S., Risi, C., and Vimeux, F. (2008), Influence of convective processes on the isotopic
626 composition (d18O and dD) of precipitation and water vapor in the tropics:1. Radiative-

627 convective equilibrium and Tropical Ocean–GlobalAtmosphere–Coupled Ocean-
628 Atmosphere ResponseExperiment (TOGA-COARE) simulations, *Journal of Geophysical*
629 *Research*, 113D19305.

630 Boucher, O. et al. (2013), Clouds and Aerosols, in *Climate Change 2013: The Physical Science*
631 *Basis. Contribution of Working Group I to the Fifth Assessment Report of the*
632 *Intergovernmental Panel on Climate Change*, pp. 571-657, Cambridge University Press,

633 Brierley, C. M. et al. (2020), Large-scale features and evaluation of the PMIP4-CMIP6
634 midHolocene simulations, *Climate of the Past Discussions*, 16(5), 1847-1872.

635 Briggs, R. D., Pollard, D., and Tarasov, L. (2014), A data-constrained large ensemble analysis of
636 Antarctic evolution since the Eemian, *Quaternary Science Reviews*, 10391-115.

637 Cai, Y. et al. (2017), Holocene moisture changes in western China, Central Asia, inferred from
638 stalagmites, *Quaternary Science Reviews*, 15815-28.

639 Caley, T., Roche, D. M., Waelbroeck, C., and Michel, E. (2014), Oxygen stable isotopes during
640 the Last Glacial Maximum climate: perspectives from data-model (iLOVECLIM)
641 comparison, *Climate of the Past*, 101939-1955.

642 Cauquoin, A., Werner, M., and Lohmann, G. (2019), Water isotopes-climate relationships for the
643 mid-Holocene and preindustrial period simulated with an isotope-enabled version of MPI-
644 ESM, *Climate of the Past*, 151913-1937.

645 Collins, M. et al. (2011), Climate model errors, feedbacks and forcings: a comparison of
646 perturbed physics and multi-model ensembles, *Climate Dynamics*, 361737-1766.

647 Comas-Bru, L. et al. (2020), SISALv2: A comprehensive speleothem isotope database with
648 multiple age-depth models, *Earth System Science Data*, 122579-2606.

649 Comas-Bru, L. et al. (2019), Evaluating model outputs using integrated global speleothem
650 records of climate change since the last glacial, *Climate of the Past*, 151157-1579.

651 Crucifix, M., and Hewitt, C. D. (2005), Impact of vegetation changes on the dynamics of the
652 atmosphere at the Last Glacial Maximum, *Climate Dynamics*, 25(5), 447-459.

653 Dansgaard, W. (1964), Stable isotopes in precipitation, *Tellus*, 16(4), 436-468.

654 Dee, S. G. et al. (2017), Improved spectral comparisons of paleoclimate models and observations
655 via proxy system modeling: Implications for multi-decadal variability, *Earth and Planetary
656 Science Letters*, 47634-46.

657 Del Genio, A. D. (2012), Representing the sensitivity of convective cloud systems to
658 tropospheric humidity in general circulation models, *Surveys in Geophysics*, 33637-656.

659 Del Genio, A. D. et al. (2015), Constraints on Cumulus Parameterization from Simulations of
660 Observed MJO Events, *Journal of Climate*, 28(16), 6419-6442, doi:10.1175/JCLI-D-11-
661 00168.1.

662 Deng, M., Mace, G. G., Wang, Z., and Berry, E. (2015), CloudSat 2C-ICE product update with a
663 new Ze parameterization in lidar-only region, *Journal of Geophysical Research:
664 Atmosphere*, 120(23), 12198-12208,
665 doi:10.1002/2015JD023600&hl=en&num=1&as_sdt=0,33.

666 Dufresne, J.-L., and Bony, S. (2008), An assessment of the primary sources of spread of global
667 warming estimates from coupled atmosphere-ocean models, *Journal of Climate*, 215135-
668 5144.

669 Duncan, D. I., and Eriksson, P. (2018), An update on global atmospheric ice estimates from
670 satellite observations and reanalyses, *Atmospheric Chemistry and Physics*.

671 Elsaesser, G. S., and Kummerow, C. D. (2015), The sensitivity of rainfall estimation to error
672 assumptions in a Bayesian passive microwave retrieval algorithm, *Journal of*
673 *Applied Meteorology and Climatology*, 54408-422.

674 Elsaesser, G. S. et al. (2017), The Multisensor Advanced Climatology of Liquid Water Path
675 (MAC-LWP), *Journal of Climate*, 3010193-10210.

676 Evans, M. N., Tolwinski-Ward, S. E., Thompson, D. M., and Anchukaitis, K. J. (2013),
677 Applications of proxy system modeling in high resolution paleoclimatology, *Quaternary*
678 *Science Reviews*, 7616-28.

679 Eyring, V. et al. (2016), Overview of the Coupled Model Intercomparison Project Phase 6
680 (CMIP6) experimental design and organization, *Geoscientific Model Development*, 91937-
681 1958.

682 Fairbanks, R. G. (1989), A 17,000-year glacio-eustatic sea level record: influence of glacial
683 melting rates on the Younger Dryas event and deep-ocean circulation, *Nature*, 342637-642.

684 Fairchild, I. J., and Baker, A. (2012), Introduction to speleothems and systems, in *Speleothem*
685 *Science: From Process to Past Environments*, edited by R. Bradley, pp. 432, Wiley-
686 Blackwell, UK.

687 Field, R. D. et al. (2014), Evaluating climate model performance in the tropics with retrievals of
688 water isotopic composition from Aura TES, *Geophysical Research Letters*, 416030-6036.

689 Flato, G. et al. (2013), Evaluation of Climate Models, in *Climate Change 2013: The Physical*
690 *Science Basis. Contribution of Working Group I to the Fifth Assessment Report of the*
691 *Intergovernmental Panel on Climate Change*, edited by T. F. Stocker et al., Cambridge
692 University Press, Cambridge, United Kingdom and New York, NY, USA.

693 Frankenberg, C. et al. (2009), Dynamic processes governing lower-tropospheric HDO/H₂O
694 ratios as observed from space and ground, *science*, 325(5946), 1374-1377.

695 Galewsky, J. et al. (2016), Stable isotopes in atmospheric water vapor and applications to the
696 hydrologic cycle, *Reviews of Geophysics*, 54809-865.

697 Gat, J. R. (1996), Oxygen and Hydrogen Isotopes in the Hydrologic Cycle, *Ann Rev Earth Planet*
698 *Sci*, 24225-262.

699 Harrison, S. P. et al. (2014), Climate model benchmarking with glacial and mid-Holocene
700 climates, *Climate Dynamics*, 43671-688.

701 Hartmann, A., and Baker, A. (2017), Modelling karst vadose zone hydrology and its relevance
702 for paleoclimate reconstruction, *Earth Science Reviews*, 172178-192.

703 Huffman, G. J., Bolvin, D. T., Nelkin, E. J., Wolff, D. B., and Adler, R. F. (2007), The TRMM
704 Multisatellite Precipitation Analysis (TMPA): Quasi-global, multiyear, combined-sensor
705 precipitation estimates at fine scales, *Journal of Hydrometeorology*, 8(1), 38-55.

706 Iguchi, T. et al. (2012), An overview of the precipitation retrieval algorithm for the Dual
707 frequency Precipitation Radar (DPR) on the Global Precipitation Measurement (GPM)
708 mission's core satellite, *Proc. SPIE 8528, Earth Observing Missions and Sensors:*
709 *Development, Implementation, and Characterization II*, 852885281C.

710 Indermühle, A. et al. (1999), Holocene carbon-cycle dynamics based on CO₂ trapped in ice at
711 Taylor Dome, Antarctica, *Nature*, 398121-126.

712 IPCC (In Press), Summary for Policymakers, in *Climate Change 2021: The Physical Science*
713 *Basis. Contribution of Working Group I to the Sixth Assessment Report of the*
714 *Intergovernmental Panel on Climate Change*, edited by V. Masson-Delmotte et al.,
715 Cambridge University Press,

716 Kageyama, M. et al. (2021), The PMIP4-CMIP6 Last Glacial Maximum experiments:
717 preliminary results and comparison with the PMIP3-CMIP5 simulations, *Climate of*
718 *the Past*, 171065-1089.

719 Kageyama, M. et al. (2017), The PMIP4 contribution to CMIP6 – Part 4: Scientific objectives
720 and experimental design of the PMIP4-CMIP6 Last Glacial Maximum experiments and
721 PMIP4 sensitivity experiments, *Geoscientific Model Development*, 10(11), 4035-4055,
722 doi:10.5194/gmd-10-4035-2017.

723 Kato, S. et al. (2018), Surface Irradiances of Edition 4.0 Clouds and the Earth’s Radiant Energy
724 System (CERES) Energy Balanced and Filled (EBAF) Data Product, *Journal of Climate*,
725 31(11), 4501-4527.

726 Kelley, M. et al. (2020), GISS-E2. 1: Configurations and climatology, *Journal of Advances in*
727 *Modeling Earth Systems*, 12(8), e2019MS002025.

728 Kim, D., and Kang, I. S. (2012), A bulk mass flux convection scheme for climate model:
729 Description and moisture sensitivity, *Climate Dynamics*, 38411-429.

730 Knutti, R., Rugenstein, M. A. A., and Hegerl, G. C. (2017), Beyond equilibrium climate
731 sensitivity, *Nature Geoscience*, 10727-736.

732 Kummerow, C. et al. (2001), The Evolution of the Goddard Profiling Algorithm (GPROF) for
733 Rainfall Estimation from Passive Microwave Sensors, *Journal of Applied Meteorology*,
734 401801-1820.

735 Lachniet, M. (2009), Climatic and environmental controls on speleothem oxygen-isotope values,
736 *Quaternary Science Reviews*, 28412-432.

737 Lee, J.-E., Pierrehumbert, R., Swann, A., and Lintner, B. R. (2009), Sensitivity of stable water
738 isotopic values to convective parameterization schemes, *Geophysical Research Letters*,
739 36L23801.

740 LeGrande, A. N., and Schmidt, G. A. (2009), Sources of Holocene variability of oxygen isotopes
741 in paleoclimate archives, *Climate of the Past*, 5441-455.

742 Licciardi, J. M., Clark, P. U., Jenson, J. W., and DR, M. (1998), Deglaciation of a soft-bedded
743 Laurentide Ice Sheet, *Quaternary Science Reviews*, 17(4-5), 427-448.

744 Licciardi, J. M., Teller, J. T., and Clark, P. U. (1999), Freshwater routing by the Laurentide Ice
745 Sheet during the last deglaciation, *Geophysical Monograph-American Geophysical Union*,
746 112177-202.

747 Liu, J., Kummerow, C. D., and Elsaesser, G. S. (2017), Identifying and analysing uncertainty
748 structures in the TRMM microwave imager precipitation product over tropical ocean
749 basins, *International Journal of Remote Sensing*, 38(1), 23-42.

750 Loeb, N. G. et al. (2018), Clouds and the Earth's Radiant Energy System (CERES) Energy
751 Balanced and Filled (EBAF) Top-of-Atmosphere (TOA) Edition-4.0 Data Product, *Journal*
752 *of Climate*, 31895-918.

753 Loeb, N. G. et al. (2020), Toward a Consistent Definition between Satellite and Model Clear-Sky
754 Radiative Fluxes, *Journal of Climate*, 3361-75, doi:10.1175/jcli-d-19-
755 0381.1.&hl=en&num=1&as_sdt=0,33.

756 Lopez, P. (2007), Cloud and precipitation parameterizations in modeling and variational data
757 assimilation: A review, *Journal of the Atmospheric Sciences*, 64(11), 3766-3784.

758 Marchant, B., Platnick, S., Meyer, K., Thomas Arnold, G., and Riedi, J. (2016), MODIS
759 Collection 6 shortwave-derived cloud phase classification algorithm and comparisons with
760 CALIOP, *Atmospheric Measurement Techniques*, 91587-1599.

761 Masson-Delmotte, V. et al. (2006), Past and future polar amplification of climate change: climate
762 model inter comparisons and ice core constraints, *Climate Dynamics*, 26513-529.

763 Mauritsen, T. et al. (2012), Tuning the climate of a global model, *Journal of Advances in*
764 *Modeling Earth Systems*, 4M00A01.

765 Meehl, G. A. et al. (2020), Context for interpreting equilibrium climate sensitivity and transient
766 climate response from the CMIP6 Earth system models, *Science Advances*, 6(26),
767 eaba1981.

768 Noone, D. (2008), The influence of midlatitude and tropical overturning circulation on the
769 isotopic composition of atmospheric water vapor and Antarctic precipitation, *Journal of*
770 *Geophysical Research*, 113D04102.

771 Nusbaumer, J., Wong, T. E., Bardeen, C., and Noone, D. (2017), Evaluating hydrological
772 processes in the Community Atmosphere Model Version 5 (CAM5) using stable isotope
773 ratios of water, *Journal of Advances in Modelling Earth Systems*, 9949-977.

774 Otto-Bliesner, B. L. et al. (2006), Last Glacial Maximum and Holocene Climate in CCSM3,
775 *Journal of Climate*, 192526-2544.

776 Otto-Bliesner, B. L. et al. (2017), The PMIP4 contribution to CMIP6 – Part 2: Two interglacials,
777 scientific objective and experimental design for Holocene and Last Interglacial simulations,
778 *Geoscientific Model Development*, 10(11), 3979-4003, doi:10.5194/gmd-10-3979-2017.

779 Pausata, F. S. R., Li, C., Wettstein, J. J., Kageyama, M., and Nisancioglu, K. H. (2011), The key
780 role of topography in altering North Atlantic atmospheric circulation during the last glacial
781 period, *Climate of the Past*, 7(4), 1089-1101.

782 Peltier, W. R. (2004), Global glacial isostasy and the surface of the ice-age Earth: the ICE-5G
783 (VM2) model and GRACE, *Annu. Rev. Earth Planet. Sci.*, 32111-149.

784 Platnick, S. et al. (2015), MODIS cloud optical properties: User guide for the Collection 6 Level-
785 2 MOD06/MYD06 product and associated Level-3 Datasets, 138.

786 Ray, N., and Adams, J. (2001), A GIS-based vegetation map of the world at the Last Glacial
787 Maximum (25,000-15,000 BP), *Internet Archaeology*, 111-44.

788 Rind, D. et al. (2020), GISS Model E2. 2: A climate model optimized for the middle
789 atmosphere—Model structure, climatology, variability, and climate sensitivity, *Journal of*
790 *Geophysical Research: Atmospheres*, 125(10), e2019JD032204.

791 Risi, C. et al. (2012), Process-evaluation of tropospheric humidity simulated by general
792 circulation models using water vapor isotopic observations: 2. Using isotopic diagnostics to
793 understand the mid and upper tropospheric moist bias in the tropics and subtropics, *Journal*
794 *of Geophysical Research*, 117D05304.

795 Rossow, W. B., and Schiffer, R. A. (1999), Advances in Understanding Clouds from ISCCP,
796 *Bulletin of the American Meteorological Society*, 80(11), 2261-2288.

797 Schmidt, G. A. et al. (2014), Using paleo-climate comparisons to constrain future projections in
798 CMIP5, *Climate of the Past*, 10221-250.

799 Schmidt, G. A., Hoffman, D. L., Shindell, D. T., and Hu, Y. (2005), Modeling atmospheric
800 stable water isotopes and the potential for constraining cloud processes and stratosphere-
801 troposphere water exchange, *Journal of Geophysical Research*, 110D21314.

802 Schmidt, G. A., LeGrande, A. N., and Hoffmann, G. (2007), Water isotope expression of
803 intrinsic and forced variability in a coupled ocean-atmosphere model, *Journal of*
804 *Geophysical Research*, 112D10103.

805 Schmidt, G. A. et al. (2017), Practice and philosophy of climate model tuning across six US
806 modeling centers, *Geoscientific Model Development*, 103207-3223.

807 Sherwood, S. C., Bony, S., and Dufresne, J.-L. (2014), Spread in model climate sensitivity traced
808 to atmospheric convective mixing, *Nature*, 50537-42.

809 Tarasov, L., Dyke, A. S., Neal, R. M., and Peltier, W. R. (2012), A data-calibrated distribution of
810 deglacial chronologies for the North American ice complex from glaciological modeling,
811 *Earth and Planetary Science Letters*, 315-31630-40.

812 Tarasov, L., and Peltier, W. R. (2002), Greenland glacial history and local geodynamic
813 consequences, *Geophysical Journal International*, 150(1), 198-229.

814 Tian, B., Fetzer, E. J., and Manning, E. M. (2019), TThe Atmospheric Infrared Sounder
815 Obs4MIPs Version 2 Data Set, *Earth and Space Science*, 6(2), 324-333,
816 doi:10.1029/2018EA000508.&hl=en&num=1&as_sdt=0,33.

817 Tian, B., and Hearty, T. (2020), Estimating and removing the sampling biases of the AIRS
818 Obs4MIPs V2 data, *Earth and Space Science*, 7(12), e2020EA001438.

819 Tierney, J. E. et al. (2020a), Glacial cooling and climate sensitivity revisited, *Nature*, 584569-
820 573.

821 Tierney, J. E. et al. (2020b), Past climates inform our future, *Science*, 370(6517).

822 Ullman, D. J., LeGrande, A. N., Carlson, A. E., Anslow, F. S., and Licciardi, J. M. (2014),
823 Assessing the impact of Laurentide Ice Sheet topography on glacial climate, *Climate of the*
824 *Past*, 10487-507.

825 Waliser, D. et al. (2020), Observations for model Intercomparison project (Obs4MIPs): Status
826 for CMIP6, *Geoscientific Model Development*, 132945-2958.

827 Waters, J. W. F., L. Harwood, R.S. Jarnot, R.F. Pickett, H.M. Read, W.G. Siegel, P.H. Cofield,
828 R.E. Filipiak, M.J. Flower, D.A. Holden, J.R. et al. (2006), The earth observing system
829 microwave limb sounder (EOS MLS) on the Aura satellite, *IEEE Transactions on*
830 *Geoscience and Remote Sensing*, 44(5), 1075-1092.

831 Webb, M. J. et al. (2015), The impact of parametrized convection on cloud feedback,
832 *Philosophical Transactions of the Royal Society A: Mathematical, Physical and*
833 *Engineering Sciences*, 373(2054), 20140414.

834 Wentz, F. J., Ricciardulli, L., Hilburn, K., and Mears, C. (2007), How Much More Rain Will
835 Global Warming Bring?, *Science*, 317(5835), 233-235.

836 Wentz, F. J., and Schabel, M. (2000), Precise climate monitoring using complementary satellite
837 data sets, *Nature*, 403414-416.

838 Werner, M. et al. (2016), Glacial-interglacial changes in H₂18O, HDO and deuterium excess -
839 results from the fully coupled ECHAM5/MPI-OM Earth system model, *Geoscientific*
840 *Model Development*, 9647-670.

841 Worden, H. M. et al. (2007), Comparisons of Tropospheric Emission Spectrometer (TES) ozone
842 profiles to ozonesondes: Methods and initial results, *Journal of Geophysical Research:*
843 *Atmospheres*, 112(D3).

844 Yi, B., Rapp, A. D., Yang, P., Baum, B. A., and King, M. D. (2017), A comparison of Aqua
845 MODIS ice and liquid water cloud physical and optical properties between collection 6 and
846 collection 5.1: Cloud radiative effects, *Journal of Geophysical Research: Atmospheres*,
847 122(8), 4550-4564.

848 Zelinka, M. D. et al. (2020), Causes of higher climate sensitivity in CMIP6 models, *Geophysical*
849 *Research Letters*, 47(1), e2019GL085782.

850 Zhu, J., Poulsen, C. J., and Tierney, J. E. (2019), Simulation of Eocene extreme warmth and high
851 climate sensitivity through cloud feedbacks, *Science Advances*, 5eaax1874.

852